MATERIALS SCIENCE

Atomic-level structure engineering of metal oxides for high-rate oxygen intercalation pseudocapacitance

Tao Ling[1,2]*, Pengfei Da[1]*, Xueli Zheng[3]*, Binghui Ge[4]*, Zhenpeng Hu[5], Mengying Wu[1], Xi-Wen Du[1], Wen-Bin Hu[1], Mietek Jaroniec[6], Shi-Zhang Qiao[1,2]†

Atomic-level structure engineering can substantially change the chemical and physical properties of materials. However, the effects of structure engineering on the capacitive properties of electrode materials at the atomic scale are poorly understood. Fast transport of ions and electrons to all active sites of electrode materials remains a grand challenge. Here, we report the radical modification of the pseudocapacitive properties of an oxide material, $Zn_xCo_{1-x}O$, via atomic-level structure engineering, which changes its dominant charge storage mechanism from surface redox reactions to ion intercalation into bulk material. Fast ion and electron transports are simultaneously achieved in this mixed oxide, increasing its capacity almost to the theoretical limit. The resultant $Zn_xCo_{1-x}O$ exhibits high-rate performance with capacitance up to 450 F g^{-1} at a scan rate of 1 V s^{-1}, competing with the state-of-the-art transition metal carbides. A symmetric device assembled with $Zn_xCo_{1-x}O$ achieves an energy density of 67.3 watt-hour kg^{-1} at a power density of 1.67 kW kg^{-1}, which is the highest value ever reported for symmetric pseudocapacitors. Our finding suggests that the rational design of electrode materials at the atomic scale opens a new opportunity for achieving high power/energy density electrode materials for advanced energy storage devices.

INTRODUCTION

A breakthrough in the development of efficient, safe, and sustainable energy storage devices for portable electronic devices, electrical vehicles, and stationary grid storage is urgently needed (*1*, *2*). Supercapacitors have become one of the most promising energy storage systems (*3*–*16*), owing to their high power density, rapid charging-discharging rate, and long cyclic stability. However, the widespread application of supercapacitors is severely limited because of intrinsically low energy density of the extensively studied carbon-based electrochemical double-layer capacitors. Recently, supercapacitors that store energy through ion intercalation into bulk electrode materials, similar to what is seen in lithium-ion batteries (LIBs), have been intensively studied (*6*–*9*, *14*, *17*–*19*). The alluring feature of this kind of supercapacitors is the promising prospect toward enhancing energy density without compromising the high power density.

Very recently, the cost-effective transition metal oxides and perovskite oxides have shown great potential in ion (cation or anion) intercalation-type supercapacitor applications (*6*–*9*, *20*–*22*). Despite great advances, the practical application of these oxide materials is still limited by their dissatisfactory rate capability, limited potential window, and low energy density (*6*, *8*, *9*). These limitations of oxide electrode materials are mainly due to the sluggish ion transport kinetics (*8*, *9*). Nanoengineering offers a novel and exciting opportunity to tackle these problems by shortening the ion transport paths and relaxing the strain generated during electrochemical cycling (*8*, *9*). These investigations indicate the opportunity of controlling the mode of charge storage by engineering proper nanostructures. However, the understanding of the ion diffusion control by atomic structure is still missing.

The inherently low electrical conductivity is another reason for the limited performance of oxide materials (*23*). Previous reports suggest that doping metal or nonmetal elements into the host oxides is an effective route to enhance their electrical conductivity (*24*), which is beneficial for achieving high energy density. Unfortunately, doping did not produce notable improvement in electrochemical performance. Even worse, it usually sacrifices the power density, which is possibly due to the nonuniform distribution of transition metal ions within oxides. Therefore, fast transport of ions and electrons to all active sites (interior and exterior) in oxide electrodes is of crucial significance for their performance, but it is still a grand challenge.

Atomic-level structure engineering can give rise to substantial modification of the chemical and physical properties of materials, which has been demonstrated with great success in the field of catalysis (*25*–*27*). So far, the atomic-level engineering and understanding of the capacitive oxide electrodes are largely missing. Here, we report the radical modification of the pseudocapacitive properties of an oxide material, $Zn_xCo_{1-x}O$, via atomic structure engineering, which changes its dominant charge storage mechanism from surface redox reactions to ion intercalation into bulk material. On the basis of the experimental observations, cutting edge characterization, and theoretical calculations, we demonstrate that atomic-level engineering endows $Zn_xCo_{1-x}O$ electrodes with both rapid ionic and electronic conductivity (Fig. 1). The creation of oxygen (O) vacancy–rich {111} nanofacets enables easy oxygen-ion intercalation into this oxide with a low energy barrier, and the atomically uniform Zn doping assures a considerable improvement of its electrical conductivity respective to pristine CoO. As a result, the $Zn_xCo_{1-x}O$ electrode exhibits high-rate performance with capacitance up to 450 F g^{-1} at a scan rate of 1 V s^{-1}, reaching the performance of the state-of-the-art transition metal carbides. A symmetric device assembled with $Zn_xCo_{1-x}O$ achieves an energy density of 67.3 watt-hour (Wh) kg^{-1}, which is the highest among symmetric pseudocapacitors consisting of metal oxides, metal sulfides, and other two-dimensional transition metal carbides.

[1]Key Laboratory for Advanced Ceramics and Machining Technology of Ministry of Education, Tianjin Key Laboratory of Composite and Functional Materials, School of Materials Science and Engineering, Tianjin University, Tianjin 300072, China. [2]School of Chemical Engineering, The University of Adelaide, Adelaide, SA 5005, Australia. [3]Department of Materials Science and Engineering, Stanford University, Stanford, CA 94305, USA. [4]Beijing National Laboratory for Condensed Matter Physics, Institute of Physics, Chinese Academy of Sciences, Beijing 100190, China. [5]School of Physics, Nankai University, Tianjin 300071, China. [6]Department of Chemistry and Biochemistry, Kent State University, Kent, OH 44242, USA.
*These authors contributed equally to this work.
†Corresponding author. Email: s.qiao@adelaide.edu.au

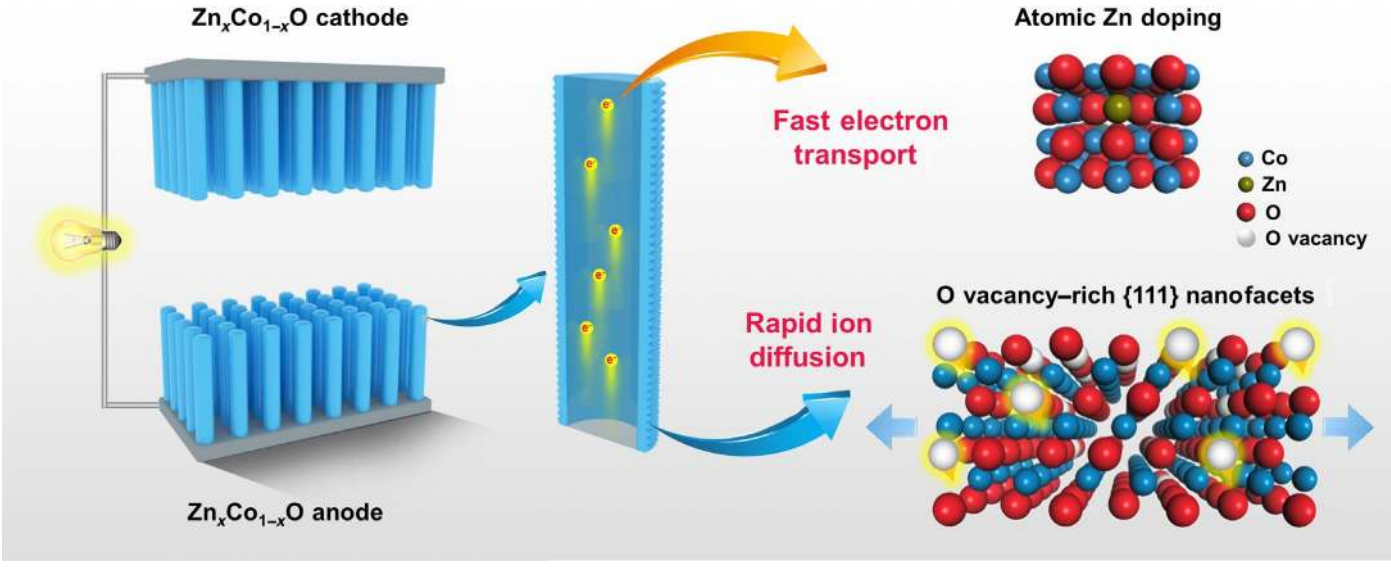

Fig. 1. Schematic diagram of the atomic-level structure engineering of $Zn_xCo_{1-x}O$ for high-rate intercalation pseudocapacitance applications. Arrays of single-crystal $Zn_xCo_{1-x}O$ nanorods (NRs) are in situ fabricated on a conductive substrate to ensure quick charge transportation. For every single $Zn_xCo_{1-x}O$ NR, the uniform doping of Zn ions in the oxide host assures fast electrical conduction, while the creation of O vacancy–rich {111} nanofacets enables easy access of oxygen ions into the oxide host with a low energy barrier.

RESULTS

Atomic structure engineering of $Zn_xCo_{1-x}O$ NRs

We fabricated arrays of $Zn_xCo_{1-x}O$ NRs in situ on carbon fiber paper (CFP) (Fig. 2A) by a cation exchange method (*28*) using ZnO NRs as sacrificial templates. This specific method enables atomically uniform Zn doping in the CoO host lattice. In traditional chemical methods, heteroatoms are generally introduced into host materials by dopant precursor incorporation during their growth. However, these methods offer poor stoichiometric and dopant distribution. In our method, we achieved the synthesis of $Zn_xCo_{1-x}O$ NRs by the replacement reaction of Co^{2+} for Zn^{2+} ions, which proceeds through inward diffusion of Co^{2+} and outward diffusion of Zn^{2+} (fig. S1). This bidirectional diffusion and similar radii of Co^{2+} and Zn^{2+} allow easy formation of a $Zn_xCo_{1-x}O$ solid solution with a single-crystal structure (Fig. 2B and figs. S2 and S3). The molar ratio of Zn^{2+} and Co^{2+} in the resultant $Zn_xCo_{1-x}O$ NRs can be easily tuned by controlling the cation exchange temperature (table S1 and figs. S3 and S4). The subnanometer spatial resolution elemental mapping shows that Co, O, and Zn elements are uniformly distributed across a single $Zn_xCo_{1-x}O$ NR (Fig. 2C and fig. S5), demonstrating that after the cation exchange process, the residual Zn^{2+} ions are well integrated into the CoO lattice, resulting in substitutional Zn^{2+} doping in CoO at the atomic level.

Moreover, the cation exchange method renders $Zn_xCo_{1-x}O$ NRs with exposed {111} nanofacets (Fig. 2D and fig. S6), which accommodate large amounts of O vacancies on the near surface region of the $Zn_xCo_{1-x}O$ NRs (fig. S7). We discerned the spatial distribution of O vacancies on the $Zn_xCo_{1-x}O$ NRs by electron energy-loss spectroscopy (EELS). Here, Co-$L_{2,3}$ edge spectra, sensitive to the presence of O vacancies, were detected along the line from site 1 to site 2 on a single $Zn_xCo_{1-x}O$ NR (Fig. 2D). The collected spectrum continuously shifts toward the high energy loss direction, indicating the gradual decrease of the amount of O vacancies, but no shift is noticed away from site 2 toward the interior of the $Zn_xCo_{1-x}O$ NRs. The peak shift observed on the two spectra collected for site 1 and site 2 is ~0.45 eV (Fig. 2E). These results reveal that the O vacancies are mostly enriched below 2 to 3 nm from the outermost surface of the $Zn_xCo_{1-x}O$ NRs with an average O vacancy concentration of ~22.5% (fig. S8 and note S1). Such high number of O vacancies induces 3 to 5% lattice expansion in the surface region of the $Zn_xCo_{1-x}O$ NRs (fig. S9). As shown below, these atomic-level structural features, i.e., abundant O vacancies confined on the {111} nanofacets and atomically uniform Zn doping, result in fast ion and electron transports in the as-engineered $Zn_xCo_{1-x}O$ NRs, which directly lead to the excellent capacitive performance.

Electrochemical properties of $Zn_xCo_{1-x}O$ NRs

To understand the influence of the above atomic-level structural characteristics on the electrochemical behavior, we measured and compared the electrochemical properties of $Zn_xCo_{1-x}O$ NRs ($x = 0$, $x = 0.04$, and $x = 0.06$) with those of polycrystalline $Zn_xCo_{1-x}O$ (P-$Zn_xCo_{1-x}O$, $x = 0.04$) NRs (figs. S10 and S11). Figure 3A shows the cyclic voltammetry (CV) curves collected at a scan rate of 50 mV s^{-1} for a voltage window of 0.8 V [−1.0 to −0.2 V versus Ag/AgCl ($V_{Ag/AgCl}$)]. Notably, P-$Zn_xCo_{1-x}O$ NRs exhibit typical redox pseudocapacitance in the potential range of −0.1 to 0.4 $V_{Ag/AgCl}$ (fig. S12A). In the potential window studied, we only observed an electric double-layer capacitance in the case of P-$Zn_xCo_{1-x}O$ NRs (Fig. 3A, figs. S12B and S13, and note S2). Unexpectedly, $Zn_xCo_{1-x}O$ NRs show nearly rectangular current-voltage curves, characteristic of an ideal pseudocapacitive response (Fig. 3A and fig. S14). Impressively, the maximum capacity of $Zn_{0.04}Co_{0.96}O$ NRs reaches as high as 1065 F g^{-1} at 5 mV s^{-1}, which is nearly 31 times higher than that of P-$Zn_xCo_{1-x}O$ NRs. Given that the Brunauer-Emmet-Teller (BET) surface area of $Zn_xCo_{1-x}O$ NRs (~30 m^2 g^{-1}) is only one-third of that measured for P-$Zn_xCo_{1-x}O$ NRs (~91 m^2 g^{-1}), the observed substantial capacity enhancement of $Zn_xCo_{1-x}O$ NRs in comparison to P-$Zn_xCo_{1-x}O$ NRs demonstrates a great feasibility to promote the charge storage of electrode materials through atomic structure engineering. The galvanostatic charge/discharge measurements with exceptional cycling stability further confirmed the excellent

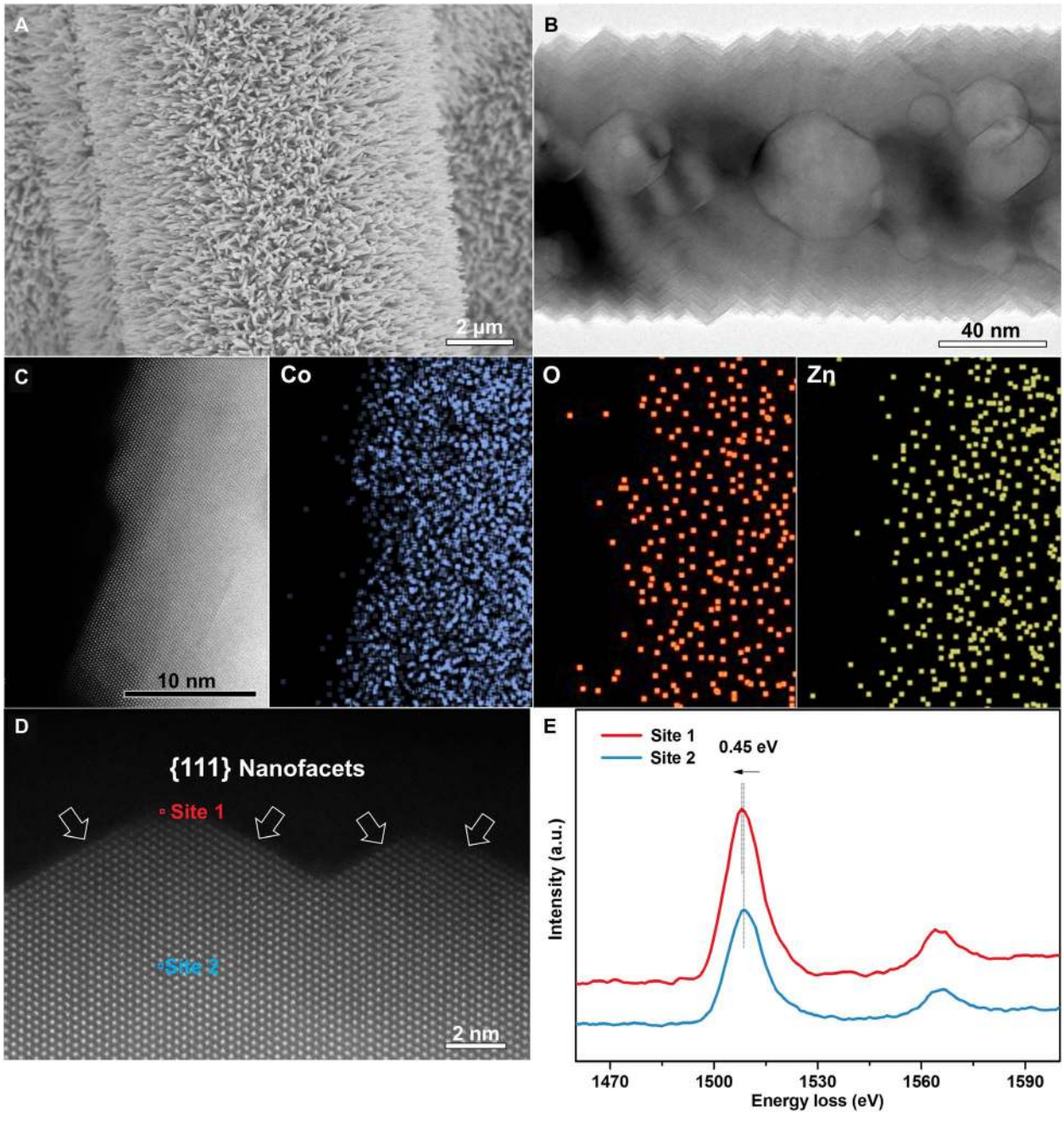

Fig. 2. Characterization of $Zn_xCo_{1-x}O$ NRs. (**A**) Typical scanning electron microscopy (SEM) image of $Zn_xCo_{1-x}O$ NR arrays distributed on CFP. (**B**) Transmission electron microscopy (TEM) image of an individual $Zn_xCo_{1-x}O$ NR. (**C**) Elemental mapping of Co, O, and Zn on a single $Zn_xCo_{1-x}O$ NR. (**D**) Atomic-resolution high-angle annular dark-field (HAADF)–scanning TEM (STEM) image of the surface, which is enclosed with {111} nanofacets. (**E**) EELS Co-$L_{2,3}$ spectra of $Zn_xCo_{1-x}O$ NR collected at two specific sites (site 1 and site 2) as indicated in (D), where a 0.45-eV peak shift toward the low energy loss direction is evident in site 1 respective to that in site 2. The data presented in this figure refer to $Zn_{0.04}Co_{0.96}O$ NRs. a.u., arbitrary units.

electrochemical performance of $Zn_xCo_{1-x}O$ NRs (Fig. 3C, figs. S15 and S16, and table S2).

Besides high capacity, $Zn_xCo_{1-x}O$ NRs exhibit exceptional rate performance. As shown in Fig. 3B, $Zn_{0.04}Co_{0.96}O$ NRs preserve 55% of the capacitance following a 100-fold scan rate increase from 5 to 500 mV s^{-1}. Even at 1 V s^{-1}, they deliver a high capacity of up to 450 F g^{-1}, competing with the state-of-the-art high-rate transition metal carbides (*18*).

To shed light on the superior high-rate capability of $Zn_xCo_{1-x}O$ NRs, we carried out an analysis of the peak current (i) dependence on the scan rate (v; fig. S17). In general, the peak current, i, is a combination of the capacitive effect (k_1v) and diffusion-controlled intercalation ($k_2v^{1/2}$) according to (*29*)

$$i(V) = k_1v + k_2v^{1/2} \quad (1)$$

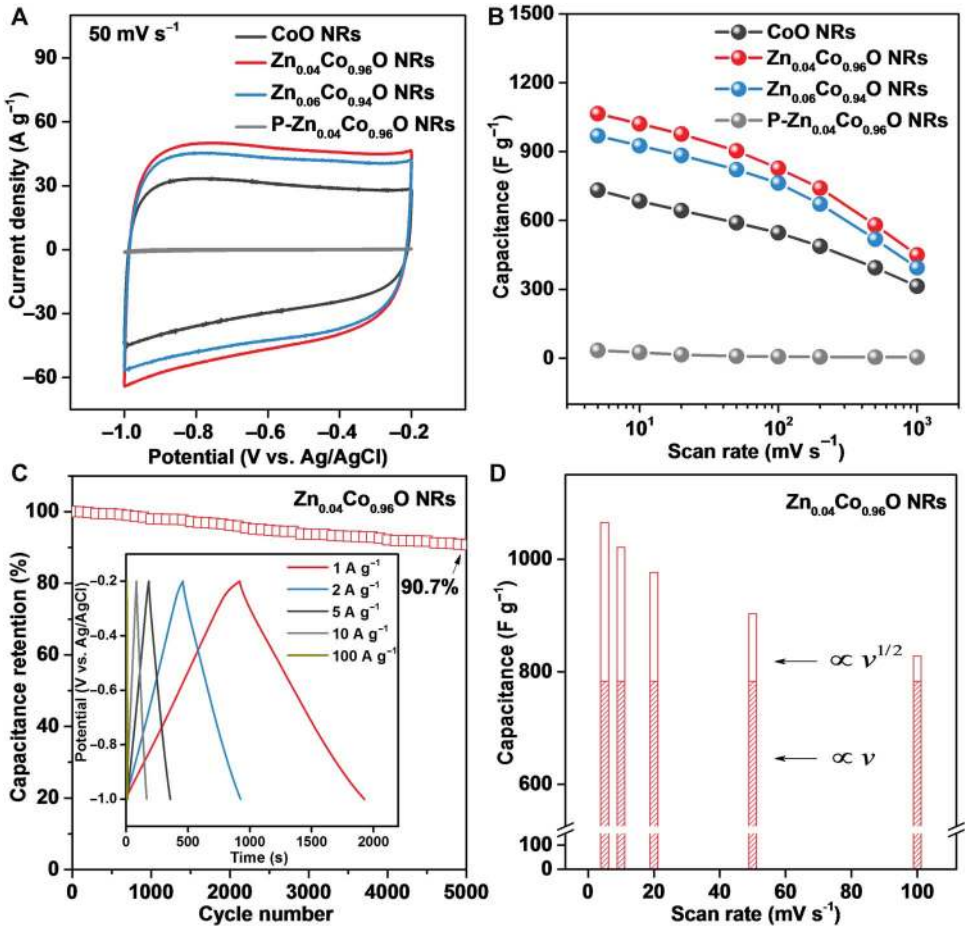

Fig. 3. Electrochemical performance of $Zn_xCo_{1-x}O$ NRs as compared with P-$Zn_xCo_{1-x}O$ NRs. (**A**) CV curves at 50 mV s^{-1}. (**B**) Specific capacity as a function of sweep rate between 5 and 1000 mV s^{-1}. (**C**) Capacitance retention of $Zn_{0.04}Co_{0.96}O$ NRs by galvanostatic cycling at 10 A g^{-1}, with the inset showing galvanostatic cycling profiles collected at 1, 2, 5, 10, and 100 A g^{-1}. (**D**) Deconvolution of the charge contribution as a function of scan rates, indicating that $Zn_{0.04}Co_{0.96}O$ NRs facilitate fast electrochemical reaction, resulting in higher capacity contributed dominantly from the *v*-dependent charge.

where *V* is a fixed potential. By determining both k_1 and k_2, it is possible to identify the fraction of current contributed by capacitive processes and that originating from diffusion-controlled intercalation. The capacitive response of the $Zn_{0.04}Co_{0.96}O$ electrode is nearly constant across a wide range of scan rates, from 5 to 100 mV s^{-1}, contributing more than 74% to the total charge storage (Fig. 3D). In contrast, the diffusion-controlled capacity is a small portion of the entire capacitance. These collective results demonstrate excellent rate performance of the $Zn_xCo_{1-x}O$ electrode, which can be ascribed to the fast ion and electron transports achieved in the as-engineered $Zn_xCo_{1-x}O$ electrodes (see discussion below).

Charge storage mechanism in $Zn_xCo_{1-x}O$ NRs

To provide further insight into the charge storage mechanism in $Zn_xCo_{1-x}O$ NRs, we performed the synchrotron-based x-ray absorption (XAS) measurements (Fig. 4A and fig. S18). The O-K edge spectra of $Zn_xCo_{1-x}O$ NRs before and after processing at −0.2 $V_{Ag/AgCl}$ are shown in Fig. 4A. A comparison of these spectra reveals the insertion of oxygen ions into the $Zn_xCo_{1-x}O$ NRs. Noticeably, peak A originates from the transition of electrons to hole states of Co3d–O2p octahedral coordination (*30*). For the as-prepared $Zn_xCo_{1-x}O$ NRs, the intensity of peak A is weak due to the presence of a large amount of O vacancies. After processing the $Zn_xCo_{1-x}O$ NRs at −0.2 $V_{Ag/AgCl}$, peak A gains intensity, indicating the increased oxygen content in the $Zn_xCo_{1-x}O$ NRs. Accordingly, shifts toward high photon energy are evident in the Co-$L_{2,3}$ edge spectra of the $Zn_xCo_{1-x}O$ NRs after processing at −0.2 $V_{Ag/AgCl}$, indicating the oxidation of Co ions (Fig. 4B). The data fitting and analysis (fig. S19) reveal that the average Co oxidation state changes per Co atom in CoO, $Zn_{0.04}Co_{0.96}O$, and $Zn_{0.06}Co_{0.94}O$ NRs are ~0.46, 0.74, and 0.72 ē, respectively (Fig. 4C). Using Faraday's law, the maximum theoretical capacity for CoO, $Zn_{0.04}Co_{0.96}O$, and $Zn_{0.06}Co_{0.94}O$ NRs can be estimated as 742, 1187, and 1153 F g^{-1}, respectively (Fig. 4C and note S3), which are in excellent agreement with the experimentally observed capacities (Figs. 3B and 4C). Therefore, the capacitive charge storage occurs dominantly by oxidation of Co ions in the bulk $Zn_xCo_{1-x}O$ through a mechanism of oxygen intercalation (note S4), which can be described as

$$Zn_xCo_{1-x}O_{1-\delta} + (2\delta + 2y)OH^- \rightleftharpoons Zn_xCo_{1-x}O_{1+y} + 2(\delta + y)e^- + (\delta + y)H_2O \quad (2)$$

where δ is the average oxygen vacancy concentration of $Zn_xCo_{1-x}O$ NRs, and *y* is the mole fraction of inserted oxygen ions beyond stoichiometry. Notably, traditional transition metal oxides, such as RuO_2,

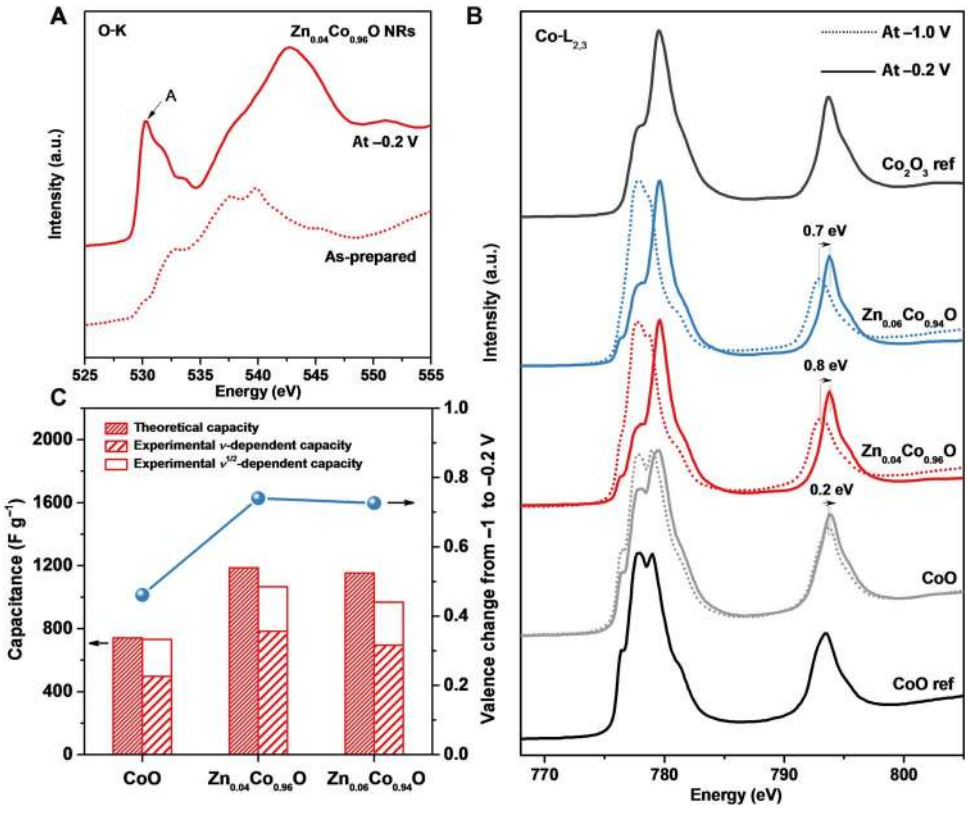

Fig. 4. Analysis of charge storage mechanism in $Zn_xCo_{1-x}O$ NRs. (**A**) O-K edge XAS spectra of $Zn_{0.04}Co_{0.96}O$ NRs before and processed at −0.2 $V_{Ag/AgCl}$. (**B**) Co-$L_{2,3}$ edge XAS spectra of $Zn_xCo_{1-x}O$ NRs collected at −1 and −0.2 $V_{Ag/AgCl}$. (**C**) Average Co oxidation state change (right) and the corresponding theoretical capacity (left) of $Zn_xCo_{1-x}O$ NRs from −1 to −0.2 $V_{Ag/AgCl}$ based on the Co-$L_{2,3}$ edge spectra fitting. The experimental charge contributions of *v*- and $v^{1/2}$-dependent capacity at 5 mV s^{-1} are shown for comparison (left).

MnO_2, and CoO_x, mainly store charges through a surface redox mechanism (*10*). In our case, the atomic-level engineering activates the oxygen intercalation, which contributes to the improved charge storage in the as-engineered $Zn_xCo_{1-x}O$ NRs. For $Zn_{0.04}Co_{0.96}O$ NRs, the obtained capacity approaches its theoretical limit of 1267 F g^{-1} (note S3). The aforementioned oxygen intercalation mechanism assures the full use of the oxide electrode.

Origin of high-rate oxygen intercalation capacitance in $Zn_xCo_{1-x}O$ NRs

Since O vacancies are the active sites for oxygen-ion intercalation, high O vacancy mobility is crucial to facilitate fast oxygen-anion intercalation during charge storage (*9*). To gain further insight into the mobility of O vacancies in the as-engineered $Zn_xCo_{1-x}O$, we carried out the first-principle calculations (fig. S20). Our results reveal that the diffusion barrier of O vacancies in $Zn_xCo_{1-x}O$ is sensitive to the surface geometrical structure. That is, O vacancies entering into the interior of $Zn_xCo_{1-x}O$ through typical low-index {100} facets encounter a high-energy barrier of 1.82 eV (Fig. 5A), well explaining why traditional $Zn_xCo_{1-x}O$ (P-$Zn_xCo_{1-x}O$) NRs exhibit negligible intercalation pseudocapacitance (Fig. 3, A and B). In contrast, the energy barrier on {111} facets falls down to 1.05 eV, and a 3% lattice expansion even gives rise to a much lower activation energy barrier of ~0.70 eV. Therefore, the {111} nanofacets and tensile strain confined on the respective surface and near surface region of $Zn_xCo_{1-x}O$ NRs provide advantageous geometrical environment for rapid diffusion of O vacancies. Moreover, the numerous nanopores inside $Zn_xCo_{1-x}O$ NRs with well-defined {111} side faces greatly enhance the surface region of $Zn_xCo_{1-x}O$ NRs (fig. S21), further facilitating the diffusion of O vacancies to all active sites inside $Zn_xCo_{1-x}O$ NRs. Note that the isolated O vacancy diffusion should vary greatly from a high concentration on the surface of $Zn_xCo_{1-x}O$. The previous work (*31*) on the cation intercalation into oxides suggests that an increase in the concentration of diffusing cation results in a decrease in the diffusion barrier. A similar situation is in our case, where diffusion of O vacancies is greatly enhanced upon increasing the surface concentration of O vacancies (note S1). Consistent with the theoretical calculations, we observe a high oxygen diffusion rate up to 1.0×10^{-10} cm^2 s^{-1} in CoO NRs (figs. S22 and S23), which is about one or two orders of magnitude higher than that observed in perovskite oxides (*9*), and even higher than the lithium diffusion rate in common lithium-ion intercalation materials (*32*).

On the other hand, only fast oxygen-ion intercalation is insufficient to achieve this high intercalation capacity in $Zn_xCo_{1-x}O$ NRs, which can be accomplished by simultaneous promotion of the electronic conductivity. As displayed by the calculated density of states (DOS) in Fig. 5B, the pristine CoO exhibits a wide bandgap of ~2.4 eV, indicating intrinsically poor electronic conductivity. For the Zn-doped CoO ($Zn_xCo_{1-x}O$), some new electronic states emerge in the bandgap (indicated by arrow in Fig. 5B). The enhanced DOS increase the carrier density in $Zn_xCo_{1-x}O$. This is supported by Mott-Schottky (M-S) measurements showing that the Zn-doped CoO NRs feature nearly 10-fold enhancement in charge carriers as compared with CoO NRs (fig. S24). This promotion of

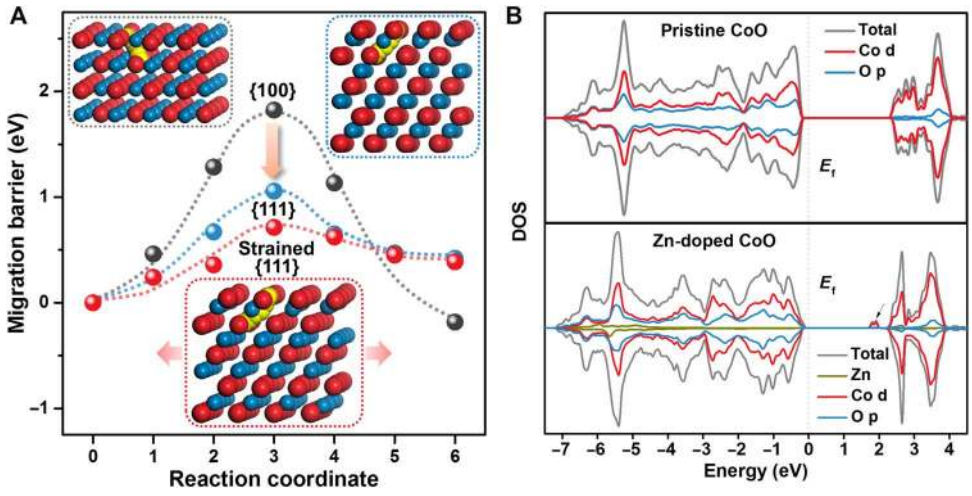

Fig. 5. Computational investigations of oxygen ion diffusion and electrical conduction in $Zn_xCo_{1-x}O$. (**A**) Migration activation energies of the O vacancy diffusing into bulk $Zn_xCo_{1-x}O$ (x = 0) through {100}, {111}, and strained {111} facets (with 3% tensile strain), with the inset showing the O vacancy diffusion path. Color codes: blue and red spheres denote cobalt and oxygen atoms, respectively, and yellow spheres denote diffusing O vacancy. (**B**) The DOS on pristine and Zn-doped CoO. The arrow points out new electronic states, which appear in the bandgap of Zn-doped CoO, demonstrating the importance of atomic Zn^{2+} doping in promoting the electrical conduction in $Zn_xCo_{1-x}O$.

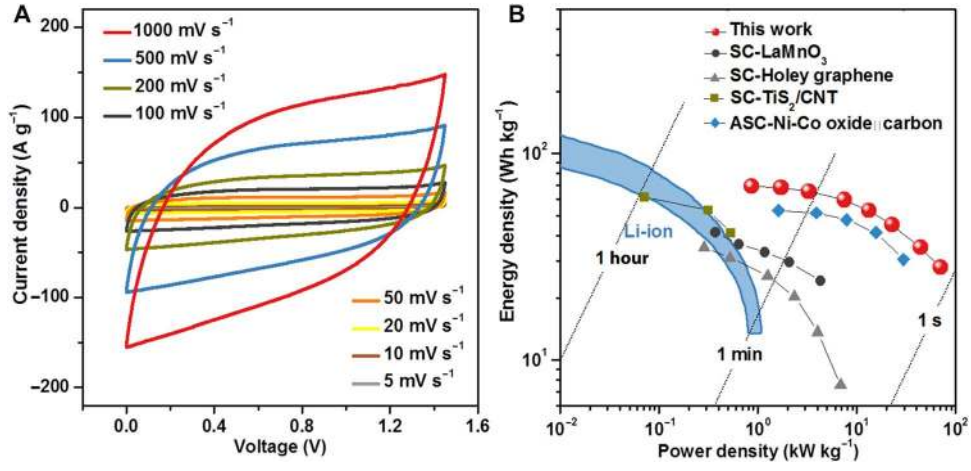

Fig. 6. Electrochemical performance of symmetric supercapacitor device in aqueous electrolyte (6 M KOH). (**A**) CV curves of our symmetric supercapacitor (SC) device at different scan rates. (**B**) Ragone plot of the SC device, data of traditional LIBs, some high-performance SCs (*9*, *35*, *36*), and asymmetric supercapacitor (ASC) (*11*) devices are also added for the purpose of comparison. Our SC device is assembled with $Zn_{0.04}Co_{0.96}O$ NR electrodes as both cathode and anode.

electronic conductivity leads directly to greatly increased capacitive charge storage in Zn-doped CoO NRs ($Zn_{0.04}Co_{0.96}O$ and $Zn_{0.06}Co_{0.94}O$ NRs) as compared with CoO NRs (Fig. 4C).

Thus, in the atomically engineered $Zn_xCo_{1-x}O$ NRs, fast ion and electron transports are simultaneously achieved and synergistically combined to contribute to their superior performance. Following this atomic engineering route, it is predicted that further charge transport promotion in this oxide can lead to the capacity exceeding 2000 F g^{-1} (note S3) without sacrificing its power capability. This ideal oxide electrode could, in principle, be realized by multielement doping and/or by decreasing the crystal size of oxide.

Practical application of $Zn_xCo_{1-x}O$ NRs in symmetric supercapacitors

Electrode materials with large potential windows are highly preferable in practical storage devices. However, oxide electrodes are usually plagued by limited potential windows. $Zn_xCo_{1-x}O$ NRs can also afford a high level of intercalation pseudocapacitance in the working potentials above 0 $V_{Ag/AgCl}$ (fig. S25). Therefore, a symmetric cell composed of two $Zn_xCo_{1-x}O$ NRs electrodes successfully extends the operating voltage window to nearly 1.5 V in aqueous electrolyte (Fig. 6A), much higher than those of the reported cobalt oxide-based electrodes (0.6 to 0.8 V) (*33*, *34*). Figure 6B shows the specific power density and energy density of the as-fabricated device in comparison to traditional LIBs. As shown, $Zn_xCo_{1-x}O$ NRs deliver a steady and high energy density over a wide range of power, presenting a high energy density of 67.3 Wh kg^{-1} at a power density of 1.67 kW kg^{-1}, approaching the higher end of LIBs. To the best of our knowledge, this is the highest value among symmetric pseudocapacitors (table S3) consisting of metal oxides (*9*), metal sulfides (*35*), and other two-dimensional materials (*36*). Even at a high power density of 68.6 kW kg^{-1}, the device still has an energy density of 27.6 Wh kg^{-1}. Therefore, our work shows the possibility of atomic-level

structure engineering of metal oxides to achieve a promising capacitive intercalation that presents both high power density and energy density.

DISCUSSION

We have demonstrated atomic-level structure engineering of a metal oxide for high-rate charge storage via oxygen intercalation. The combination of experiment and theoretical calculations shows that the excellent performance can be assigned to the simultaneously enhanced ionic diffusion and electronic conductivity in the as-engineered oxide studied. The confinement of abundant O vacancies on {111} nanofacets enables easy intercalation of oxygen ions into this oxide with a low energy barrier, and the atomically uniform Zn doping assures fast electrical conduction. We emphasize that the as-engineered oxide electrode exhibits high rate capability, a wide potential window, and high energy density, with its maximum capacity approaching the theoretical limit. We believe that this work will stimulate research toward atomic-level structure engineering of electrode materials, which can be used to design the next-generation high energy and high power electrochemical devices.

MATERIALS AND METHODS

Synthesis of $Zn_xCo_{1-x}O$ NRs and P-$Zn_xCo_{1-x}O$ NRs

In this work, the self-supported $Zn_xCo_{1-x}O$ NR arrays were grown directly on CFP using a cation exchange method in the gas phase (*37*–*39*). ZnO NRs on CFP were used as sacrificial templates. The molar ratio of Zn^{2+} and Co^{2+} in the resultant $Zn_xCo_{1-x}O$ NRs can be easily controlled by tuning the cation exchange temperature (table S1). P-$Zn_xCo_{1-x}O$ NRs were fabricated on CFP using the hydrothermal method (*40*). Zinc nitrate [$Zn(NO_3)_2$] was chosen as the zinc dopant precursor, and the molar ratio of Zn^{2+} and Co^{2+} in the final P-$Zn_xCo_{1-x}O$ NRs was tuned by tuning the mass ratio of Zn^{2+} and Co^{2+} in the precursors.

Structural characterizations

SEM and TEM characterizations were carried out using a Hitachi S-4800 SEM and a JEOL 2100 TEM, respectively. HAADF-STEM imaging was performed on a JEOL ARM200F microscope with a STEM aberration corrector operated at 200 kV. The BET surface area was determined from nitrogen adsorption data measured at 77 K on an ASAP 2020 physisorption analyzer (Micromeritics Inc., USA). The loading masses of $Zn_xCo_{1-x}O$ and P-CoO NRs on CFP substrates were measured using inductively coupled plasma mass spectrometry (NexION 300Q, PerkinElmer).

XAS measurements

XAS measurements were carried out at experimental station 8-2 of the Stanford Synchrotron Radiation Light Source. XAS data were recorded in fluorescence yield mode. $Zn_xCo_{1-x}O$ electrodes were processed using CV. After five cycles with the scan rate of 10 mV s^{-1}, the electrode was cycled at 5 mV s^{-1} to the required potential. The electrodes were then taken out from the electrolyte, washed with ethanol, dried using argon gas, and then sealed in tape to prevent exposure to the environment.

Electrochemical characterizations

Electrochemical measurements were carried out using a VersaSTAT 3 electrochemistry workstation from Princeton Applied Research. The tests were performed in a standard three-electrode electrochemical cell using oxide NR-loaded CFP as the working electrode, an Ag/AgCl electrode as the reference electrode, and a Pt wire as the counter electrode in nitrogen gas saturated with 6 M KOH electrolyte. The capacitive property of CFP is provided in fig. S26. The loading amounts of CoO, $Zn_{0.04}Co_{0.96}O$, $Zn_{0.06}Co_{0.94}O$, and P-$Zn_{0.04}Co_{0.96}O$ NRs on the CFP substrate were 0.322, 0.326, 0.356, and 0.335 mg cm^{-2}, respectively. In the symmetric device testing, one $Zn_xCo_{1-x}O$ NR electrode acted as the working electrode, and the other served as the counter electrode. The total loading mass of $Zn_xCo_{1-x}O$ NRs on these two electrodes was 0.652 mg cm^{-2}.

Computational methods

All density functional theory (DFT) computations were performed with the Hubbard-U framework (DFT + U) using the Vienna ab initio simulation package. The projector-augmented wave pseudopotential with the Perdew-Burke-Ernzerhof exchange-correlation functional was used in the computations. The Hubbard effective term U_{eff}(Co) = 3.7 eV was applied. The relevant details, references, and computational structural models (figs. S20 and S27) are given in the Supplementary Materials.

SUPPLEMENTARY MATERIALS

Supplementary material for this article is available at http://advances.sciencemag.org/cgi/content/full/4/10/eaau6261/DC1

Fig. S1. Schematic diagram of the cation exchange methodology for the synthesis of $Zn_xCo_{1-x}O$ NRs.
Fig. S2. TEM characterizations of $Zn_xCo_{1-x}O$ NRs.
Fig. S3. X-ray diffraction (XRD) spectra of $Zn_xCo_{1-x}O$ NRs.
Fig. S4. SEM images of $Zn_xCo_{1-x}O$ NRs.
Fig. S5. Composition analysis of a single $Zn_{0.04}Co_{0.96}O$ NR.
Fig. S6. HAADF-STEM characterization of the as-exchanged $Zn_xCo_{1-x}O$ NRs.
Fig. S7. X-ray photoelectron spectroscopy O 1s spectra of $Zn_xCo_{1-x}O$ NRs.
Fig. S8. Schematic illustration of the spatial distribution of O vacancies in a single $Zn_xCo_{1-x}O$ NR.
Fig. S9. Analysis of lattice expansion of the surface region of $Zn_xCo_{1-x}O$ NRs.
Fig. S10. Characterization of P-$Zn_xCo_{1-x}O$ NRs fabricated directly on CFP.
Fig. S11. XRD spectrum of P-$Zn_xCo_{1-x}O$ NRs fabricated on CFP.
Fig. S12. CV curves of P-$Zn_xCo_{1-x}O$ NRs.
Fig. S13. Atom arrangements on low index planes of CoO.
Fig. S14. CV curves of $Zn_xCo_{1-x}O$ NRs collected at scan rates from 5 to 1000 mV s^{-1}.
Fig. S15. XPS spectra of $Zn_{0.04}Co_{0.96}O$ NRs before and after the cycling test.
Fig. S16. Structural characterizations of $Zn_{0.04}Co_{0.96}O$ NRs after the cycling test.
Fig. S17. Deconvolution of diffusion-controlled and capacitive-like capacitance in $Zn_xCo_{1-x}O$ NRs.
Fig. S18. O-K edge x-ray absorption near-edge structure spectra of $Zn_xCo_{1-x}O$ NRs before and processed at −0.2 $V_{Ag/AgCl}$.
Fig. S19. Analysis of Co-$L_{2,3}$ edge XAS spectra of $Zn_xCo_{1-x}O$ NRs.
Fig. S20. Top-view and side-view illustration of O vacancy diffusion path through different surface facets.
Fig. S21. TEM image of an individual $Zn_xCo_{1-x}O$ NR.
Fig. S22. Length distribution of $Zn_xCo_{1-x}O$ NRs fabricated directly on CFP.
Fig. S23. Diffusion rate calculations for $Zn_xCo_{1-x}O$ NRs.
Fig. S24. M-S plots for $Zn_xCo_{1-x}O$ NRs.
Fig. S25. Electrochemical performance of $Zn_xCo_{1-x}O$ NRs as compared with P-$Zn_xCo_{1-x}O$ NRs.
Fig. S26. CV curve of carbon fiber paper.
Fig. S27. Simulation models of bulk CoO and Zn-doped CoO.
Table S1. Average O vacancy concentrations of $Zn_xCo_{1-x}O$ NRs.
Table S2. Elemental analysis of $Zn_{0.04}Co_{0.96}O$ NRs before and after the cycling test.
Table S3. Comparative summary of the performance of $Zn_xCo_{1-x}O$ NRs in symmetric supercapacitor with the present symmetric supercapacitor and asymmetric supercapacitors.
Note S1. Analysis of the distribution of O vacancy on $Zn_xCo_{1-x}O$ NRs.
Note S2. Estimation of the theoretical capacitance of P-$Zn_xCo_{1-x}O$ NRs.
Note S3. Estimation of the theoretical capacitance of $Zn_xCo_{1-x}O$ NRs.
Note S4. Analysis of the oxygen intercalation mechanism in $Zn_xCo_{1-x}O$ NRs.
Supplementary Methods

REFERENCES AND NOTES

1. B. Dunn, H. Kamath, J.-M. Tarascon, Electrical energy storage for the grid: A battery of choices. *Science* **334**, 928–935 (2011).
2. Z. Yang, J. Zhang, M. C. W. Kintner-Meyer, X. Lu, D. Choi, J. P. Lemmon, J. Liu, Electrochemical energy storage for green grid. *Chem. Rev.* **111**, 3577–3613 (2011).
3. C.-C. Hu, K.-H. Chang, M.-C. Lin, Y.-T. Wu, Design and tailoring of the nanotubular arrayed architecture of hydrous RuO_2 for next generation supercapacitors. *Nano Lett.* **6**, 2690–2695 (2006).
4. X. Lang, A. Hirata, T. Fujita, M. Chen, Nanoporous metal/oxide hybrid electrodes for electrochemical supercapacitors. *Nat. Nanotechnol.* **6**, 232–236 (2011).
5. M. Toupin, T. Brousse, D. Bélanger, Charge storage mechanism of MnO_2 electrode used in aqueous electrochemical capacitor. *Chem. Mater.* **16**, 3184–3190 (2004).
6. V. Augustyn, J. Come, M. A. Lowe, J. W. Kim, P.-L. Taberna, S. H. Tolbert, H. D. Abruña, P. Simon, B. Dunn, High-rate electrochemical energy storage through Li^+ intercalation pseudocapacitance. *Nat. Mater.* **12**, 518–522 (2013).
7. T. Brezesinski, J. Wang, S. H. Tolbert, B. Dunn, Ordered mesoporous α-MoO_3 with iso-oriented nanocrystalline walls for thin-film pseudocapacitors. *Nat. Mater.* **9**, 146–151 (2010).
8. H.-S. Kim, J. B. Cook, H. Lin, J. S. Ko, S. H. Tolbert, V. Ozolins, B. Dunn, Oxygen vacancies enhance pseudocapacitive charge storage properties of MoO_{3-x}. *Nat. Mater.* **16**, 454–460 (2017).
9. J. T. Mefford, W. G. Hardin, S. Dai, K. P. Johnston, K. J. Stevenson, Anion charge storage through oxygen intercalation in $LaMnO_3$ perovskite pseudocapacitor electrodes. *Nat. Mater.* **13**, 726–732 (2014).
10. P. Simon, Y. Gogotsi, Materials for electrochemical capacitors. *Nat. Mater.* **7**, 845–854 (2008).
11. B. Y. Guan, A. Kushima, L. Yu, S. Li, J. Li, X. W. Lou, Coordination polymers derived general synthesis of multishelled mixed metal-oxide particles for hybrid supercapacitors. *Adv. Mater.* **29**, 1605902 (2017).
12. B. Y. Guan, L. Yu, X. Wang, S. Song, X. W. Lou, Formation of onion-like $NiCo_2S_4$ particles via sequential ion-exchange for hybrid supercapacitors. *Adv. Mater.* **29**, 1605051 (2017).
13. D. Choi, G. E. Blomgren, P. N. Kumta, Fast and reversible surface redox reaction in nanocrystalline vanadium nitride supercapacitors. *Adv. Mater.* **18**, 1178–1182 (2006).
14. M. R. Lukatskaya, O. Mashtalir, C. E. Ren, Y. Dall'Agnese, P. Rozier, P. L. Taberna, M. Naguib, P. Simon, M. W. Barsoum, Y. Gogotsi, Cation intercalation and high volumetric capacitance of two-dimensional titanium carbide. *Science* **341**, 1502–1505 (2013).
15. W. Sugimoto, H. Iwata, K. Yokoshima, Y. Murakami, Y. Takasu, Proton and electron conductivity in hydrous ruthenium oxides evaluated by electrochemical impedance spectroscopy: The origin of large capacitance. *J. Phys. Chem. B* **109**, 7330–7338 (2005).
16. C. Sassoye, C. Laberty, H. L. Khanh, S. Cassaignon, C. Boissière, M. Antonietti, C. Sanchez, Block-copolymer-templated synthesis of electroactive RuO_2-based mesoporous thin films. *Adv. Funct. Mater.* **19**, 1922–1929 (2009).
17. D. Kundu, B. D. Adams, V. Duffort, S. H. Vajargah, L. F. Nazar, A high-capacity and long-life aqueous rechargeable zinc battery using a metal oxide intercalation cathode. *Nat. Energy* **1**, 16119 (2016).
18. M. R. Lukatskaya, S. Kota, Z. Lin, M.-Q. Zhao, N. Shpigel, M. D. Levi, J. Halim, P.-L. Taberna, M. W. Barsoum, P. Simon, Y. Gogotsi, Ultra-high-rate pseudocapacitive energy storage in two-dimensional transition metal carbides. *Nat. Energy* **2**, 17105 (2017).
19. M. Ghidiu, M. R. Lukatskaya, M.-Q. Zhao, Y. Gogotsi, M. W. Barsoum, Conductive two-dimensional titanium carbide 'clay' with high volumetric capacitance. *Nature* **516**, 78–81 (2014).
20. K. Naoi, T. Kurita, M. Abe, T. Furuhashi, Y. Abe, K. Okazaki, J. Miyamoto, E. Iwama, S. Aoyagi, W. Naoi, P. Simon, Ultrafast nanocrystalline-TiO_2 (B)/carbon nanotube hyperdispersion prepared via combined ultracentrifugation and hydrothermal treatments for hybrid supercapacitors. *Adv. Mater.* **28**, 6751–6757 (2016).
21. L. Zhu, Y. Liu, C. Su, W. Zhou, M. Liu, Z. Shao, Perovskite $SrCo_{0.9}Nb_{0.1}O_{3-\delta}$ as an anion-intercalated electrode material for supercapacitors with ultrahigh volumetric energy density. *Angew. Chem. Int. Ed.* **55**, 9576–9579 (2016).
22. T. Zhai, S. Sun, X. Liu, C. Liang, G. Wang, H. Xia Achieving insertion-like capacity at ultrahigh rate via tunable surface pseudocapacitance. *Adv. Mater.* **30**, 1706640 (2018).
23. M. Park, X. Zhang, M. Chung, G. B. Less, A. M. Sastry, A review of conduction phenomena in Li-ion batteries. *J. Power Sources* **195**, 7904–7929 (2010).
24. Y. Li, P. Hasin, Y. Wu, $Ni_xCo_{3-x}O_4$ nanowire arrays for electrocatalytic oxygen evolution. *Adv. Mater.* **22**, 1926–1929 (2010).
25. C. Chen, Y. Kang, Z. Huo, Z. Zhu, W. Huang, H. L. Xin, J. D. Snyder, D. Li, J. A. Herron, M. Mavrikakis, M. Chi, K. L. More, Y. Li, N. M. Markovic, G. A. Somorjai, P. Yang, V. R. Stamenkovic, Highly crystalline multimetallic nanoframes with three-dimensional electrocatalytic surfaces. *Science* **343**, 1339–1343 (2014).
26. K. Ariga, S. Ishihara, H. Abe, Atomic architectonics, nanoarchitectonics and microarchitectonics for strategies to make junk materials work as precious catalysts. *CrystEngComm* **18**, 6770–6778 (2016).
27. H. Abe, J. Liu, K. Ariga, Catalytic nanoarchitectonics for environmentally compatible energy generation. *Mater. Today* **19**, 12–18 (2016).
28. J. B. Rivest, P. K. Jain, Cation exchange on the nanoscale: An emerging technique for new material synthesis, device fabrication, and chemical sensing. *Chem. Soc. Rev.* **42**, 89–96 (2013).
29. A. J. Bard, L. R. Faulkner, *Electrochemical Methods: Fundamentals and Applications* (Wiley, ed. 2, 2001).
30. L. Karvonen, M. Valkeapää, R.-S. Liu, J.-M. Chen, H. Yamauchi, M. Karppinen, O-*K* and Co-*L* XANES study on oxygen intercalation in perovskite $SrCoO_{3-\delta}$. *Chem. Mater.* **22**, 70–76 (2010).
31. H. Yildirim, J. Greeley, S. K. R. S. Sankaranarayanan, Effect of concentration on the energetics and dynamics of Li ion transport in anatase and amorphous TiO_2. *J. Phys. Chem. C* **115**, 15661–15673 (2011).
32. M. G. S. R. Thomas, P. G. Bruce, J. B. Goodenough, Lithium mobility in the layered oxide $Li_{1-x}CoO_2$. *Solid State Ion.* **17**, 13–19 (1985).
33. C. Zhou, Y. Zhang, Y. Li, J. Liu, Construction of high-capacitance 3D CoO@polypyrrole nanowire array electrode for aqueous asymmetric supercapacitor. *Nano Lett.* **13**, 2078–2085 (2013).
34. R. B. Rakhi, W. Chen, D. Cha, H. N. Alshareef, Substrate dependent self-organization of mesoporous cobalt oxide nanowires with remarkable pseudocapacitance. *Nano Lett.* **12**, 2559–2567 (2012).
35. X. Zang, C. Shen, E. Kao, R. Warren, R. Zhang, K. S. Teh, J. Zhong, M. Wei, B. Li, Y. Chu, M. Sanghadasa, A. Schwartzberg, L. Lin, Titanium disulfide coated carbon nanotube hybrid electrodes enable high energy density symmetric pseudocapacitors. *Adv. Mater.* **30**, 1704754 (2018).
36. Y. Xu, Z. Lin, X. Zhong, X. Huang, N. O. Weiss, Y. Huang, X. Duan Holey graphene frameworks for highly efficient capacitive energy storage. *Nat. Commun.* **5**, 4554 (2014).
37. C. Meng, T. Ling, T.-Y. Ma, H. Wang, Z. Hu, Y. Zhou, J. Mao, X.-W. Du, M. Jaroniec, S.-Z. Qiao, Atomically and electronically coupled Pt and CoO hybrid nanocatalysts for enhanced electrocatalytic performance. *Adv. Mater.* **29**, 1604607 (2017).
38. T. Ling, D.-Y. Yan, Y. Jiao, H. Wang, Y. Zheng, X. Zheng, J. Mao, X.-W. Du, Z. Hu, M. Jaroniec, S.-Z. Qiao, Engineering surface atomic structure of single-crystal cobalt (II) oxide nanorods for superior electrocatalysis. *Nat. Commun.* **7**, 12876 (2016).
39. T. Ling, D.-Y. Yan, H. Wang, Y. Jiao, Z. Hu, Y. Zheng, L. Zheng, J. Mao, H. Liu, X.-W. Du, M. Jaroniec, S.-Z. Qiao, Activating cobalt(II) oxide nanorods for efficient electrocatalysis by strain engineering. *Nat. Commun.* **8**, 1509 (2017).
40. H. Zhang, T. Ling, X.-W. Du, Gas-phase cation exchange toward porous single-crystal CoO nanorods for catalytic hydrogen production. *Chem. Mater.* **27**, 352–357 (2015).

Acknowledgments

Funding: This work was supported by the National Science Fund for Excellent Young Scholars (51722103), the Natural Science Foundation of China (51571149 and 21576202), the Joint Funds of the National Natural Science Foundation of China and Guangdong Province (U1601216), and the Australian Research Council (ARC) through the Discovery Project program (FL170100154, DP170104464, and DP160104866). XAS measurements were carried out at Stanford Synchrotron Radiation Lightsource, SLAC National Accelerator Laboratory. The calculations were performed on TianHe-1A at the National Supercomputer Center, Tianjin.

Author contributions: T.L. and S.-Z.Q. conceived the project and designed the experiments. T.L., P.D., and M.W. performed the experiments. T.L. and B.G. carried out the TEM characterization. X.Z. performed the soft XAS characterization. Z.H. and T.L. conducted the DFT calculations. All authors discussed the results and commented on or prepared the manuscript. **Competing interests:** The authors declare that they have no competing interests. **Data and materials availability:** All data needed to evaluate the conclusions in the paper are present in the paper and/or the Supplementary Materials. Additional data related to this paper may be requested from the authors.

Submitted 29 June 2018
Accepted 12 September 2018
Published 19 October 2018
10.1126/sciadv.aau6261

Citation: T. Ling, P. Da, X. Zheng, B. Ge, Z. Hu, M. Wu, X.-W. Du, W.-B. Hu, M. Jaroniec, S.-Z. Qiao, Atomic-level structure engineering of metal oxides for high-rate oxygen intercalation pseudocapacitance. *Sci. Adv.* **4**, eaau6261 (2018).

Atomic-level structure engineering of metal oxides for high-rate oxygen intercalation pseudocapacitance

Tao Ling, Pengfei Da, Xueli Zheng, Binghui Ge, Zhenpeng Hu, Mengying Wu, Xi-Wen Du, Wen-Bin Hu, Mietek Jaroniec and Shi-Zhang Qiao

Sci Adv **4** (10), eaau6261.
DOI: 10.1126/sciadv.aau6261